AIMS Geosciences

AIMS Geosciences, 9(1): 153–183.
DOI: 10.3934/geosci.2023009
Received: 27 November 2022
Revised: 24 January 2023
Accepted: 07 February 2023
Published: 22 February 2023

http://www.aimspress.com/journal/geosciences

Research article

Theoretical evaluation of the power efficiency of a moored hybrid floating platform for wind and wave energy production in the Greek seas

Kimon Kardakaris[1,*], Dimitrios N Konispoliatis[1] and Takvor H Soukissian[2]

[1] Laboratory for Floating Structures and Mooring Systems, Division of Marine Structures, School of Naval Architecture and Marine Engineering, National Technical University of Athens, 9 Heroon Polytechniou Avenue, GR 157–73 Athens, Greece
[2] Institute of Oceanography, Hellenic Centre for Marine Research, 190 13 Anavyssos, Greece

* **Correspondence:** Email: kimonkard@gmail.com; Tel: +2107721420.

Abstract: In this study, an extreme value analysis of wind and wave parameters is presented for three specific locations in the Greek seas that are known to be advantageous in terms of joint power production (both offshore wind and wave) and bathymetric conditions. The analysis is conducted via the Peak-Over-Threshold method, examining wind speed, significant wave height and peak wave period data from the ERA5 reanalysis dataset. Moreover, a multi-purpose floating platform suitable for offshore energy production is presented, which combines wind and wave energy resources exploitation and can be adequately utilized at the selected locations. The analysis is built to incorporate the solutions of the diffraction, motion-dependent and pressure-dependent radiation problems around the floating structure, along with the mooring line and wind turbine (WT) characteristics. Subsequently, a coupled hydro-aero-elastic analysis was performed in the frequency domain, while a dynamic analysis was conducted in order to evaluate the mooring characteristics. Lastly, offshore wind output and absorbed wave energy values were estimated, and different types of mooring systems were compared in terms of efficiency. It has been concluded that the wind energy capacity factor is higher than 50% in all the examined locations, and by the mooring system comparison, the tension-leg platform (TLP) represents the best-case scenario for wave energy absorption.

Keywords: multi-purpose floating platform; catenary mooring line system; hybrid wind-wave energy; extreme value analysis; Greek seas

1. Introduction

Over the last decades, it is more and more evident that the global energy demands are rapidly increasing. This, along with the imminent fossil fuel deficiency, oblige governments and industries to make accelerated efforts toward producing green energy. The main focus is the marine environment, which is a vast source of renewable energy. The Global Offshore Wind Report of 2021 [1] from the Global Wind Energy Council (GWEC) states that from now to 2050, offshore wind is becoming the main medium for global decarbonization, transforming the electricity system in generation and infrastructure, as well as for production of green fuels like hydrogen. Offshore wind is a key technology in net zero scenarios, with fixed-bottom offshore wind being in rapid development until 2030 and floating offshore wind unlocking tremendous potential for fossil fuel displacement from 2030 and beyond.

Even though the majority of offshore wind farms consist of fixed-bottom structures, with the advances of technology into deeper waters, floating wind turbine platforms are capable of becoming more financially profitable due to the extreme abundance of the offshore wind potential [2]. Numerous concepts and projects of floating offshore wind turbines (FOWTs) have been studied and tested, such as the GustoMSC Tri-Floater [3], WindFloat [4], TetraSpar [5], NAUTILUS-10 [6], OC4-DeepCWind and OC5 [7,8]. There are also concepts that aim to integrate other forms of energy, such as wave energy, into a single system, through multi-purpose floating structures, or to integrate multiple wind turbines (WTs) together on a single platform [9]. Although hybrid systems capable of capturing simultaneously wind and wave energy sources are still far from commercial use (only a few concepts [10–12] have been reported in the marine sector), numerous studies on hybrid systems have been presented in the literature. Specifically, several wave energy absorption technologies, i.e., attenuators, point absorbers and flap type converters, have been coupled with FOWTs. For example, Bachynski and Moan [13] examined a combined energy system consisting of a wind turbine with three point absorber wave energy converters (WEC) installed on a tension-leg floating structure. Muliawan et al. [14,15] studied a combination of a spar-type floating turbine with Wavebob, i.e., a torus-shaped WEC, while Veigas and Iglesias [16] assessed the performance of a collocated wind and wave farm in Tenerife. Moreover, Michailides et al. [17,18] studied the combination of a semisubmersible wind turbine with three rotating flap-type WECs, and Gao et al. [19] compared the spar torus combination with the latter. Karimirad and Koushan [20] analyzed the dynamic response of a hybrid system based on the Hywind concept and a Wavestar type WEC. Finally, Wang et al. [21,22] assessed the responses of the combination of a spar-type floating wind turbine with a torus-shaped WEC [21] and of a floating wind turbine with three oscillating floater WECs [22].

In addition to the aforementioned wave energy absorption technologies, the Oscillating Water Column (OWC) systems are among the most widely studied solutions for coupled wind and wave energy conversion systems. Particularly, focusing on the last decade, Aubault et al. [23] studied the effect of the Power-Take-Off (PTO) on the inner free surface of an OWC device when it is considered as part of a FOWT system. In addition, Mazarakos et al. [24] presented a coupled hydro-aero-elastic analysis in the frequency and time domains concerning a hybrid TLP supporting a 5 MW WT and encompassing three OWC devices. The latter study was further extended by Mazarakos et al. [25], with scaled-down tank tests to extrapolate the effect of the air turbine type at the top of the OWC chambers to the platform's seakeeping. Perez-Collazo et al. [26] investigated experimentally a Jacket hybrid frame substructure, incorporating a WT and an OWC device, whereas Perez-Collazo et al. [27]

examined an offshore wind monopile platform type integrating an OWC, considering regular and irregular waves. Sarmiento et al. [28] validated experimentally the hydrodynamic performance of a semisubmersible hybrid platform, encompassing three OWCs and a 5MW WT, moored with a catenary line system. Michele et al. [29] assessed the interaction effects of an OWC monopile system, supporting a WT, with regular and random waves. It was shown that the characteristics of the oscillating chambers affect the wave power extraction efficiency, whereas the presence of the internal cylindrical pile affects the sloshing eigenfrequencies. Furthermore, Zhou et al. [30] examined the wave loads on a monopile-mounted WT encompassing an OWC using a 3-D time domain numerical model. Recently, a multi-purpose floating TLP concept, named the REFOS platform, consisting of three OWCs and a 10 MW WT, was numerically and experimentally examined. In the latter studies, a hydro-servo-aero-elastic coupled model was developed in the time domain to examine the effect of the WT on the floater's seakeeping, [31–33].

Despite the fact that FOWTs are in the path of becoming competitive in the energy market, bearing in mind that they are extensively developed, tested and validated, it is critical to further improve cost-wise factors. The main disadvantage compared to onshore wind farms is that offshore wind turbines are more expensive and difficult to install and maintain, due to the variable and rough sea conditions, construction and operation phases, as well as additional infrastructure regarding the electricity transmission to shore [34]. One of these key factors that necessitate optimization and further research for economy is the mooring system of the structure. In this work, the Renewable Energy Multi-Purpose Floating Offshore System (REFOS) platform [31–33] will be utilized for wind and wave energy exploitation in specific locations in the Greek seas. An extreme value analysis will be also conducted in order to determine the designated range of environmental conditions at the installation sites. Additionally, a catenary mooring system will be specified and compared with the initial TLP arrangement in terms of power efficiency, while the energy output will be estimated for the selected locations. The current study can initiate further research and investigation in the field of offshore energy in the Greek Seas, prioritizing the trade-off between power efficiency and financial feasibility for commercial use of moored hybrid floating platforms that produce green energy.

The present manuscript is structured as follows: In Section 2 the wind and wave climate analysis for the potential installation locations in the Greek Seas are presented, whereas Section 3 deals with the hydrodynamic analysis of the floating structure. The analysis is implemented in the frequency domain, involving the solution of the coupled hydro-aero-elastic problem of the floater, the WT, the OWCs and the mooring system. In Section 4 the hydrodynamic behavior of the floating structure is presented in detail, and Section 5 is dedicated to the estimation of the absorbed wind and wave energy by the floating platform. The conclusions are presented in Section 6.

2. Environmental elements

In this section, apart from the presentation of areas in the Greek seas suitable for offshore wind and wave co-exploitation, an extreme value analysis will be performed on metocean parameters. The results along with the sea-state frequency tables, will enable the definition of the mooring characteristics in ultimate limit states and the energy output estimation of the installed system.

2.1. Site selection and data

Offshore wind provides a more powerful source of energy than onshore wind. Focusing in the Mediterranean Sea, studies have shown that in terms of Levelized Cost of Energy (LCOE), the lowest values refer to the Gulf of Lion and the Aegean Sea (approximately 95 €/MWh), where the wind resource is the best [35]. The offshore wind power potential of the Aegean and Ionian Seas has been analytically studied by Soukissian et al. [36], including annual and inter-annual variability characteristics using a 15-year hindcast of wind data. It is concluded that offshore deep-water locations, especially in the Aegean Sea, are characterized by high values of offshore wind resources (mean annual wind power density up to 885 W/m^2 in the central Aegean and up to 584 W/m^2 in the Ionian Sea). Due to the fact that the main concept of the present paper is to assess a multi-purpose floating structure in order to capture both wind and wave energy, the temporal relations between the two phenomena are also critical. Such study for the Greek Seas has been presented by Kardakaris et al. [37], in order to assess the complementarity and synergy between wind and waves and depict the most promising areas using EMODnet bathymetry [38]. In this context, three offshore locations were selected at approximately 200 m of water depth (Figure 1). The first location (L1) is east of Cyclades complex and south of Ikaria Isl. [37.220° N, 26.115° E] (at 230 m water depth), the second one (L2) is between Kythira Isl. and Antikythera Isl. [35.964° N, 23.160° E] (at 208m water depth), and the third site (L3) is located between Kasos Isl. and Karpathos Isl. [35.378° N, 27.038° E] (at 246 m water depth).

In this work, 20 years (2000–2019) of the ERA5 reanalysis wind and wave datasets [39] with a time step of one hour have been utilized for the Greek Seas (defined by a rectangle with the top left corner at 42° N, 19° E and bottom right corner at 33° N, 30° E). For the significant wave height and the wave energy period, the data are provided on a 0.50° × 0.50° spatial grid, while for the wind speed, the data are available at 100 m height (i.e., at a typical wind turbine hub height) on a 0.25° × 0.25° spatial grid. The ERA5 reanalysis dataset, produced by the European Centre for Medium-Range Weather Forecasts (ECMWF), combines vast amounts of historical observations into global estimates using advanced modeling and data assimilation systems [39]. Further works regarding sensitivity testing between the ERA5 wind and wave data and in-situ measurements can be found in [40–43].

2.2. Data preparation and sea-state tables

The ERA5 reanalysis dataset was spatially co-located with the selected locations via the nearby grid point values by using a simple form of inverse squared distance weighting interpolation function based on the values of the four nearest grid points. Denoting by x_1, x_2, x_3 and x_4 the respective variables (wind or wave parameters) at the four grid points surrounding the selected location and by r_1, r_2, r_3 and r_4 the corresponding distances from that location, the requested data for each variable at the specific site can be estimated as follows:

$$x = \frac{\sum_{i=1}^{4} \frac{x_i}{r_i^2}}{\sum_{i=1}^{4} \frac{1}{r_i^2}} \quad (1)$$

Regarding the wave data, the ERA5 reanalysis dataset refers to the wave energy period T_e. Under the JONSWAP spectrum with a peak enhancement factor γ=3.3, T_p and T_e are approximately related as follows:

$$\frac{T_e}{T_p} \approx 0.9 \tag{2}$$

In Tables 1–3 the sea-state occurrences for locations L1, L2 and L3 are respectively presented.

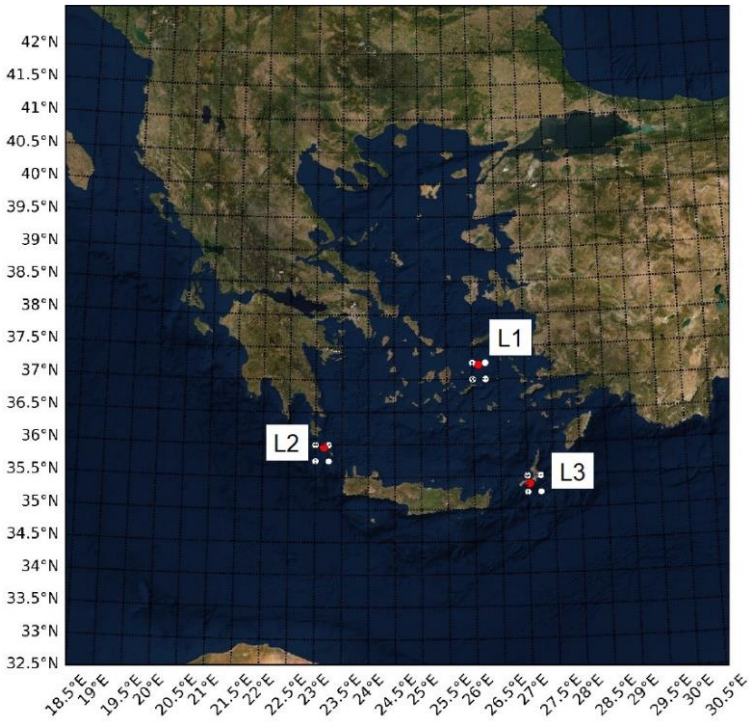

Figure 1. Selected locations in the Aegean Sea.

Table 1. Sea-state occurrences of location L1 analyzing 20-year data of 1-hour timestep. (Highest value is depicted in bold).

Peak Wave Period T_p (s)	Significant Wave Height H_s (m)					
	0–1	1–2	2–3	3–4	4–5	5–6
1–2	3	0	0	0	0	0
2–3	5948	0	0	0	0	0
3–4	41945	9	0	0	0	0
4–5	**48280**	16770	0	0	0	0
5–6	6733	39206	1053	0	0	0
6–7	118	3321	9563	157	0	0
7–8	1	74	569	1294	64	0
8–9	0	0	1	34	157	13
9–10	0	0	0	0	1	6
10–11	0	0	0	0	0	0
11–12	0	0	0	0	0	0

Table 2. Sea-state occurrences of location L2 analyzing 20-year data of 1-hour timestep. (Highest value is depicted in bold).

Peak Wave Period T_p (s)	Significant Wave Height H_s (m)					
	0–1	1–2	2–3	3–4	4–5	5–6
1–2	11	0	0	0	0	0
2–3	597	0	0	0	0	0
3–4	17707	2	0	0	0	0
4–5	**51890**	8266	0	0	0	0
5–6	23392	30663	412	0	0	0
6–7	3893	15396	7895	72	0	0
7–8	309	3949	4515	1609	44	0
8–9	1	839	1421	963	377	19
9–10	0	107	381	315	119	15
10–11	0	0	48	48	21	8
11–12	0	0	0	2	4	10

Table 3. Sea-state occurrences of location L3 analyzing 20-year data of 1-hour timestep. (Highest value is depicted in bold).

Peak Wave Period T_p (s)	Significant Wave Height H_s (m)					
	0–1	1–2	2–3	3–4	4–5	5–6
1–2	0	0	0	0	0	0
2–3	12	0	0	0	0	0
3–4	11284	0	0	0	0	0
4–5	**63374**	1932	0	0	0	0
5–6	27057	46706	32	0	0	0
6–7	2121	13860	6033	10	0	0
7–8	12	472	1424	900	7	0
8–9	0	0	4	46	34	0
9–10	0	0	0	0	0	0
10–11	0	0	0	0	0	0
11–12	0	0	0	0	0	0

2.3. Extreme value analysis (EVA)

In general, design parameters corresponding to environmental loads implied by wind, waves, currents, ice, etc. are used to evaluate the resistance of an offshore structure in the ultimate limit state, whereas the accurate estimation of design values greatly facilitates the analysis of different serviceability limit states and fatigue. In this respect, a bivariate EVA of wind and waves can produce 50- or 100-year return forces that would be experienced by a typical offshore system. Regarding EVA methods, the most widely used are the Block Maxima (BM) and the Peaks-Over-Threshold (POT). The latter will be used in this work for the EVA of the wave parameters for the examined locations, since the available sample size of annual maxima is rather poor (20 years) [44,45]. More applications regarding the estimation of metocean extremes can be found in [46–48]. A similar study has been

conducted by Devis-Morales *et al.* [49] for the offshore Colombian Caribbean Sea, where a 24-year dataset of Cross-Calibrated Multi-Platform (CCMP) winds and a 35-year dataset of ERA-Interim significant wave heights were analyzed via BM method, POT method and the Method of Independent Storm (MIS). Further applications of the POT method can be found both regionally, e.g., with H_s data of Figueira da Foz, Portugal [50], and globally for ocean wind speed and H_s, estimating 100-year return periods from a 46-year ERA-40 dataset [51]. POT method has been also used for estimation of long-term trends in the frequency and intensity of severe storm waves [52], as well as for developing extremes' modeling, capturing both short- and long-range correlations with a fitted autoregressive fractionally integrated moving average (ARFIMA) model [53].

2.3.1. Peaks-over-threshold method and model diagnostics

In the present work, the Peaks-Over-Threshold method is utilized. For a detailed description of the method, see Coles [54]. The main challenge in the POT method is to choose a threshold u that balances bias and variance. Too low a threshold is likely to violate the asymptotic basis of the model, leading to bias, whereas too high a threshold will generate few excesses with which the model can be estimated, leading to high variance. In this context, two approaches are available for threshold selection: One is an exploratory technique carried out prior to model estimation; the other is an assessment of the stability of parameter estimates, based on the fitting of models across a range of different thresholds [55]. Regarding the first approach, theory suggests that when the generalized Pareto distribution is appropriate, the sample mean of the threshold excesses of u changes linearly with u. This leads to the mean residual life (MRL) plot, which constitutes the locus of points

$$\left\{\left(u, \frac{1}{n_u}\sum_{i=1}^{n_u}\left(x_{(i)}-u\right)\right): u < x_{max}\right\}, \tag{3}$$

where $x_{(1)}, \ldots, x_{(n_u)}$ consist of the n_u observations that exceed u, and x_{max} is the largest of the $x_{(i)}$. Above a threshold u_0 at which the generalized Pareto distribution provides a valid approximation to the excess distribution, the MRL plot should be approximately linear in u. In the second approach for threshold selection, the aim is to estimate the model at a range of thresholds and to look for stability of parameter estimates. This argument suggests plotting both $\sigma^* = \sigma_u - \xi u$ (modified scale) and ξ (shape) estimates of the generalized Pareto distribution against u, together with confidence intervals for each of these quantities, and selecting u_0 as the lowest value of u for which the estimates remain near-constant. The parameters of the generalized Pareto distribution can be estimated by the Maximum Likelihood (ML) method.

In offshore and coastal engineering applications, the concept of return period and design value is chosen as common practice to adequately cover the ultimate limit state scenarios. The formal definition of the return period implies that the n −year design value is expected to be exceeded on average once during the next n years. The period of n years is called the return period, associated with the design value [54]. In this case, the N-year return level z_N is estimated through the following relation:

$$z_N = u + \frac{\sigma}{\xi}\left[\left(Nn_y\zeta_u\right)^{\xi} - 1\right], \tag{4}$$

Where ζ_u denotes the exceedance probability or the proportion of data above a threshold u, and n_y denotes the exceedance observations per year. When $\xi = 0$, equation (4) simplifies as follows:

$$z_N = u + \sigma \log\left(N n_y \zeta_u\right). \tag{5}$$

The quality of the fitted generalized Pareto model can be assessed by probability (PP) and quantile (QQ) plots. For a threshold u, threshold excesses $y_{(1)} \leq \ldots \leq y_{(n)}$ and an estimated model $\hat{H}$, the probability plot consists of the pairs

$$\left\{\left(\frac{i}{k+1}, \hat{H}\left(y_{(i)}\right)\right); i = 1, \ldots, k\right\}, \tag{6}$$

where

$$\hat{H}(y) = 1 - \left(1 + \frac{\hat{\xi} y}{\hat{\sigma}}\right)^{-1/\hat{\xi}}, \tag{7}$$

while the quantile plot constitutes the locus of points

$$\left\{\left(\hat{H}^{-1}\left(\frac{i}{k+1}\right), y_{(i)}\right); i = 1, \ldots, k\right\}, \tag{8}$$

where

$$\hat{H}^{-1}(y) = u + \frac{\hat{\sigma}}{\hat{\xi}}\left[y^{-\hat{\xi}} - 1\right], \tag{9}$$

provided that $\hat{\xi} \neq 0$. If $\hat{\xi} = 0$ the equations (7) and (9) are modified, accordingly, as follows:

$$\hat{H}(y) = 1 - exp\left(-\frac{y}{\hat{\sigma}}\right), \quad y > 0, \tag{10}$$

$$\hat{H}^{-1}(y) = u - \hat{\sigma} \log(y), \quad y > 0, \tag{11}$$

Provided that both plots depict a very close relation between theoretical and sample quantities, the model diagnostics are completed, and the model is adequately identified.

2.3.2. EVA results

After the necessary modifications in the datasets described in section 2.2 and the methodology presented in (2.3.1), an EVA on significant wave height (H_s), peak wave period (T_p) and wind speed (U_w) at 100 m above sea level was performed for the three examined locations via a Python script based on [55].

The first step of the analysis is to select an appropriate threshold level. For that purpose, the MRL plot (Figure 2) and the shape (ξ) and modified scale (σ^*) stability plots (Figure 3) were used. The threshold u should be located at the end of the linear part of the curve in the MRL plot and on the constant part of both stability plots [54]. Regarding the first plot, it is linear approximately up to $u \approx 13$, and then it curves and returns to linearity for u between 18 and 22. Based on this behavior, a threshold of 15, 18, 20 or 22 can be potentially selected. However, when stability plots are taken into account, the error bars above the threshold u = 18 become significant, suggesting an increased

variance in this interval. Although a fair selection is u = 15, as it meets all the aforementioned requirements, a slightly higher threshold was selected (u = 17.5) after trials, as it did not negate the variance prerequisites and provided more consistent results, as will be discussed below. Besides, such approach is in favor of safety when designing a project, since EVA results are utilized for robustness in ultimate limit states. A similar procedure was followed for all locations, and the resulting thresholds are shown in Table 4.

Table 4. Thresholds for every examined parameter and location.

Location	U_W	H_S	T_P
L1	17.5 m/s	3 m	7 s
L2	18.5 m/s	3.25 m	8.5 s
L3	18 m/s	2.75 m	7 s

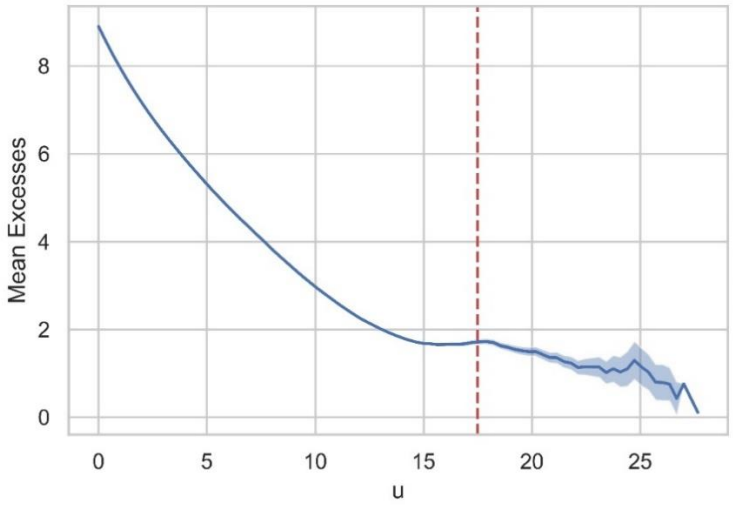

Figure 2. MRL plot with confidence bands of U_w (m/s) for L1. Red line depicts the threshold selection.

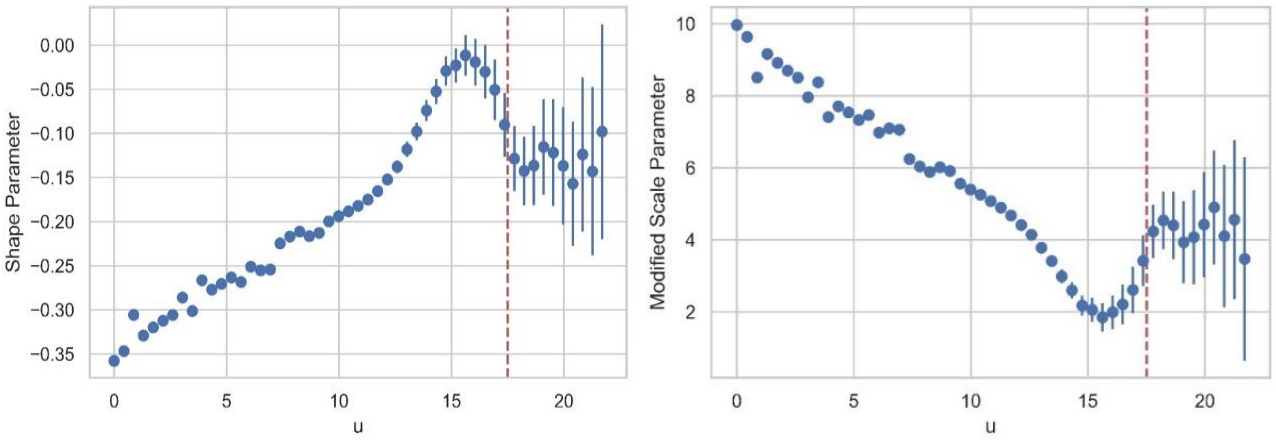

Figure 3. Shape stability plot (left) and modified scale stability plot (right) with error bars of U_w (m/s) for L1. Red line depicts the threshold selection.

Having selected the thresholds, diagnostic plots for the fitted generalized Pareto model are shown in Figures 4 and 5. None of the plots gives any real cause for concern about the quality of the fitted model, which supports the bias-variance trade-off. Furthermore, the confidence bands at the return level plot are rather narrow.

The extracted return values of wind speed at location L1 for 20–100 year return periods are shown in the right panel of Figure 5, along with the corresponding error bars. All the relevant results are also summarized in Tables 5–7. For location L3, the return levels of the wave parameters are smaller compared to the locations L2 and L3. Regarding wind speed, location L1 exhibits the largest design values compared to L2 and L3, as location L1 is characterized by strong winter and summer winds (Etesian winds).

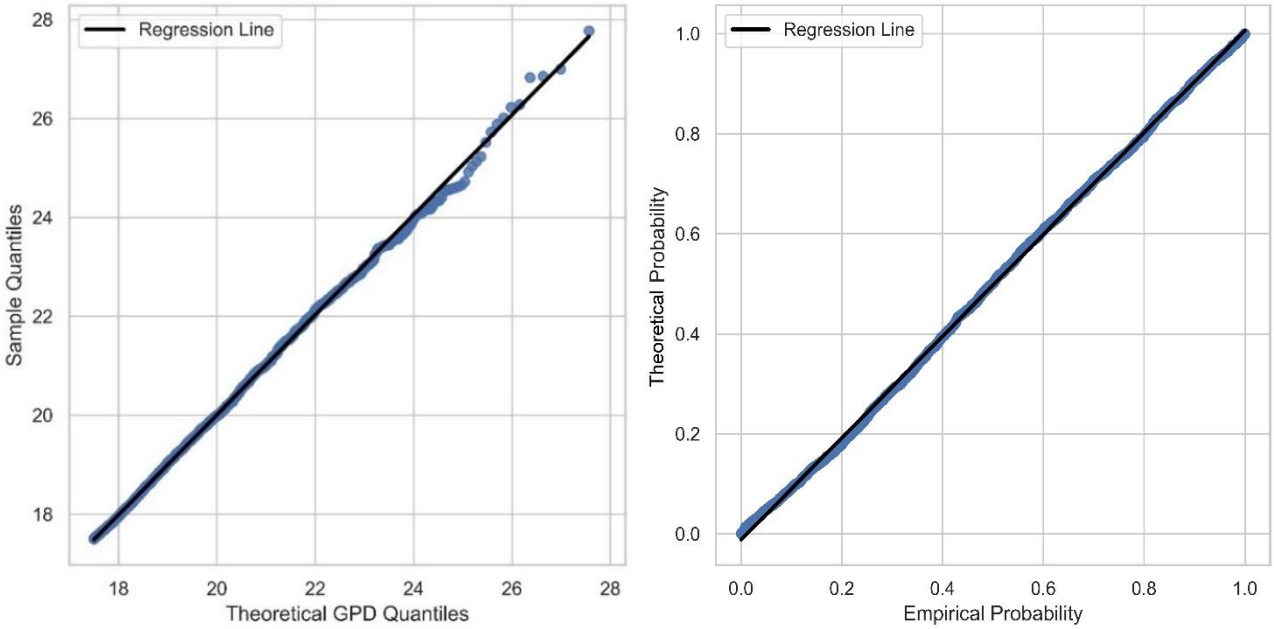

Figure 4. QQ plot (left) and PP plot (right) of U_w for L1.

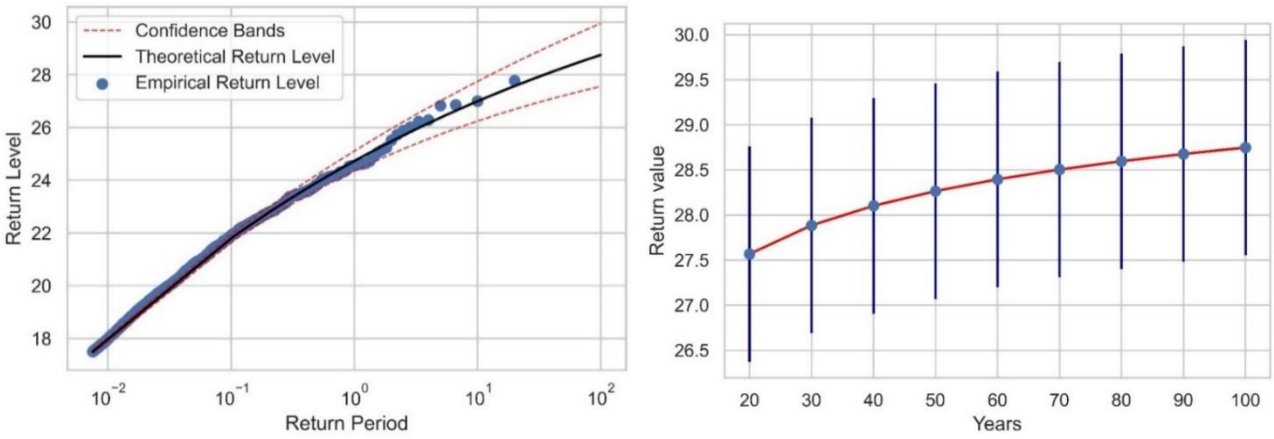

Figure 5. Return level plot with confidence bands (left) and return values curve with error bars (right) of U_w for L1.

Table 5. Return values and 95% confidence intervals of U_w (m/s) referring to the three presented locations.

Years	*Location 1*		*Location 2*		*Location 3*	
	Ret. Level	95% Conf. Int.	Ret. Level	95% Conf. Int.	Ret. Level	95% Conf. Int.
20	27.57	[26.69, 28.45]	26.51	[25.89, 27.12]	24.20	[23.61, 24.80]
30	27.88	[26.93, 28.85]	26.67	[26.01, 27.32]	24.37	[23.72, 25.01]
40	28.10	[27.09, 29.12]	26.77	[26.09, 27.46]	24.48	[23.79, 25.16]
50	28.27	[27.21, 29.32]	26.85	[26.14, 27.56]	24.56	[23.85, 25.27]
60	28.40	[27.30, 29.49]	26.91	[26.18, 27.64]	24.62	[23.89, 25.35]
70	28.50	[27.38, 29.63]	26.96	[26.22, 27.71]	24.67	[23.92, 25.42]
80	28.60	[27.45, 29.75]	27.00	[26.24, 27.76]	24.72	[23.95, 25.48]
90	28.68	[27.50, 29.85]	27.04	[26.27, 27.81]	24.75	[23.97, 25.53]
100	28.75	[27.55, 29.94]	27.07	[26.29, 27.85]	24.79	[23.99, 25.58]

Table 6. Return values and 95% confidence intervals of H_s (m) referring to the three presented locations.

Years	*Location 1*		*Location 2*		*Location 3*	
	Ret. Level	95% Conf. Int.	Ret. Level	95% Conf. Int.	Ret. Level	95% Conf. Int.
20	6.01	[5.63, 6.38]	6.22	[5.94, 6.50]	4.43	[4.33, 4.54]
30	6.13	[5.71, 6.54]	6.31	[6.01, 6.62]	4.46	[4.35, 4.58]
40	6.21	[5.77, 6.66]	6.37	[6.05, 6.70]	4.48	[4.36, 4.60]
50	6.28	[5.81, 6.74]	6.42	[6.09, 6.76]	4.50	[4.37, 4.62]
60	6.33	[5.84, 6.82]	6.46	[6.11, 6.81]	4.51	[4.38, 4.64]
70	6.37	[5.87, 6.87]	6.49	[6.13, 6.85]	4.51	[4.38, 4.65]
80	6.41	[5.89, 6.93]	6.52	[6.15, 6.89]	4.52	[4.39, 4.66]
90	6.44	[5.91, 6.97]	6.54	[6.17, 6.92]	4.53	[4.39, 4.66]
100	6.47	[5.93, 7.01]	6.56	[6.18, 6.94]	4.53	[4.40, 4.67]

Table 7. Return values and 95% confidence intervals of T_p (s) referring to the three presented locations.

Years	*Location 1*		*Location 2*		*Location 3*	
	Ret. Level	95% Conf. Int.	Ret. Level	95% Conf. Int.	Ret. Level	95% Conf. Int.
20	9.39	[9.16, 9.61]	11.74	[11.48, 12.00]	8.43	[8.35, 8.52]
30	9.46	[9.21, 9.71]	11.84	[11.56, 12.12]	8.45	[8.36, 8.55]
40	9.51	[9.25, 9.77]	11.90	[11.61, 12.20]	8.47	[8.37, 8.56]
50	9.55	[9.28, 9.82]	11.95	[11.65, 12.26]	8.48	[8.38, 8.58]
60	9.58	[9.30, 9.86]	11.99	[11.67, 12.31]	8.49	[8.39, 8.59]
70	9.60	[9.31, 9.89]	12.02	[11.70, 12.35]	8.49	[8.39, 8.60]
80	9.62	[9.33, 9.92]	12.05	[11.72, 12.38]	8.50	[8.39, 8.60]
90	9.64	[9.34, 9.95]	12.08	[11.74, 12.41]	8.50	[8.40, 8.61]
100	9.66	[9.35, 9.97]	12.10	[11.75, 12.44]	8.51	[8.40, 8.61]

3. Multi-purpose floating platform and mooring system

In order to exploit both offshore wind and wave energy via an individual structure, the Renewable Energy Floating Offshore System (REFOS) [31–33] is selected to be installed at the three examined locations presented in the previous section. The REFOS platform consists of a main cylindrical column supporting the DTU 10 MW reference wind turbine (RWT) [56] and three oscillating water column (OWC) WECs in a triangular configuration placed at the corners of the platform. Each OWC comprises an internal offset vertical cylinder and an external coaxial cylindrical shell. In the annulus area formed between the two solids, oscillations of the water column are developed. Consequently, the produced air volume flow generates an air turbine, located at the chamber's top, which is coupled to an electric generator (see Figure 6). The initial design ensures station-keeping via three lines spread symmetrically about the structure's vertical axis, which are located at the bottom of the OWCs' offset columns. In Table 8 the geometric characteristics of the examined platform are summarized, whereas its mooring properties are presented in Table 9.

Figure 6. The examined REFOS multi-purpose floating structure.

Table 8. REFOS platform: Geometric characteristics [31].

Floater		Wind Turbine	
Radius of each OWC offset column	7 m	Tower height above SWL	115.63 m
Draft of each OWC offset column	20 m	Rotor diameter	178.3 m
Radius of each OWC cylindrical cell	15.5 m	Height of the connection point between WT and floater above SWL	10 m
Draft of each OWC cylindrical cell	8 m	Hub height above SWL	129 m
Thickness of each OWC oscillating chamber	1.5 m	Mass of the WT	1,100 t
Radius of the cylindrical body supporting the WT	6 m	Fairleads distance from the seabed	~ 180 m
Draft of the cylindrical body supporting the WT	20 m	Water depth at the installation locations	~ 200 m
Mass of the floater	7,541 t		

Table 9. REFOS platform: Mooring characteristics [31].

Number of mooring lines	3
Mooring line length	~180 m
Line radius	0.61 m
Line thickness	0.042 m
Pretension of each line	18,838 kN
Young's modulus of elasticity	200 GPa
Yield stress	482.5 MPa
Mooring line stiffness k_{xx}	104 kN/m
Mooring line stiffness k_{zz}	173,533 kN/m

3.1. Hydrodynamic formulation

The detailed hydrodynamic problem has been reported extensively in [31–33]. Nevertheless, for completeness, a short outline of the relevant formulation is presented below.

The floating platform is considered to be excited by a plane periodic wave of amplitude $H/2$, wave frequency ω and wave number k. The water depth, which is assumed as constant, is $d = 200$ m. Small amplitude, inviscid, incompressible and irrotational flow are assumed so that linear potential theory can be employed. A global Cartesian co-ordinate system O-XYZ with origin on the seabed and its vertical axis directed positive upwards is used. The system coincides with the vertical axis of the central cylindrical body, which supports the WT. Also, four local cylindrical co-ordinate systems (r_q, θ_q, z_q), q=1,2,3,4 are located on the seabed with their vertical axes pointing upwards. The latter coincides with the vertical axis of q solid, q =1,2,3,4 (i.e., three OWCs and one central cylindrical body). The fluid flow around each q body, defined by $\Phi^q(r_q, \theta_q, z_q, t) = Re\{\varphi^q(r_q, \theta_q, z_q)e^{-i\omega t}\}$, can be written as

$$\varphi^q = \varphi_D^q + \sum_{p=1}^{4}\sum_{j=1}^{6} \dot{\xi}_{j0}^p \varphi_j^{qp} + \sum_{p=1}^{3} p_0^p \varphi_P^{qp}, \quad (12)$$

where φ_D^q denotes the diffraction potential around the q body when the latter is considered fixed in the wave impact, with inner atmospheric air pressure head. The φ_j^{qp} stands for the motion radiation

potential around the q body, due to the forced oscillation of the p body in the j direction, with unit velocity amplitude ξ_{j0}^{p}. Here, the air pressure inside the OWC chambers is also assumed equal to the atmospheric. The term φ_P^{qp} denotes the pressure radiation potential around the q body, due to unit time harmonic oscillating pressure head p_0^p in the p OWC device. Here, the bodies q and p are considered fixed to the wave train.

The velocity potentials $\varphi_D^q\,(q=1,..,4), \varphi_j^{qp}(q,p=1,\dots,4; j=1,\dots,6), \varphi_p^{qp}(q=1,\dots,4; p=1,2,3)$ have to satisfy the Laplace equation in the fluid domain and the following boundary conditions.
On the seabed ($z=0$),

$$\frac{\partial \varphi_D^q}{\partial z}=0, q=1,..,4,$$
$$\frac{\partial \varphi_j^{qp}}{\partial z}=0, q,p=1,..,4, j=1,\dots,6;\ \frac{\partial \varphi_p^{qp}}{\partial z}=0, q=1,..,4, p=1,2,3. \tag{13}$$

On the mean wetted surface,

$$\frac{\partial \varphi_D^q}{\partial \vec{n}^q}=0, q=1,..,4,$$
$$\frac{\partial \varphi_j^{qp}}{\partial \vec{n}^q}=\delta_{q,p} n_j^p, q,p=1,..,4, j=1,\dots,6;\ \frac{\partial \varphi_p^{q}}{\partial \vec{n}^q}=0, q=1,..,4, p=1,2,3. \tag{14}$$

At the outer free surface of each body ($z=200$),

$$\omega^2 \varphi_D^q - g\frac{\partial \varphi_D^q}{\partial z}=0, q=1,..,4,$$
$$\omega^2 \varphi_j^{qp} - g\frac{\partial \varphi_j^{qp}}{\partial z}=0, qp=1,..,4; j=1,\dots,6, \tag{15}$$
$$\omega^2 \varphi_p^{qp} - g\frac{\partial \varphi_p^{qp}}{\partial z}=0, q=1,..,4; p=1,2,3.$$

At the inner free surface of each device ($z=200$),

$$\omega^2 \varphi_p^{qp} - g\frac{\partial \varphi_p^{qp}}{\partial z}=-\delta_{p,q}\frac{i\omega}{\rho}, q=1,..,4; p=1,2,3. \tag{16}$$

In Equation (14), the term $\partial()/\partial\vec{n}^q$ stands for the derivative in the direction of the outward unit normal vector $\vec{n}^q$ to the mean body's wetted surface. The term n_j^p denotes the generalized normal components defined as $\vec{n}^p=(n_1^p,n_2^p,n_3^p)$ and $\vec{r}^p\times\vec{n}^p=(n_4^p,n_5^p,n_6^p)$, where $\vec{r}^p$ is the position vector with respect to the origin of the coordinate system. Finally, a radiation condition should be fulfilled, which states that the propagating disturbances must be outgoing.

The velocity potentials $\varphi_D^q,\ \varphi_j^{qp}, \varphi_p^{qp}$ are evaluated through the method of matched axisymmetric eigenfunction expansions. Hence, the fluid field around each solid can be subdivided into coaxial ring-shaped regions in which different expressions of the velocity potential can be established. These velocity potential solutions are matched by the continuity requirements of the hydrodynamic pressure and radial velocity along vertical boundaries of adjacent fluid regions and the fulfillment of the kinematic boundary condition at the bodies' vertical walls. Regarding the wave interaction phenomena between the array's members and the incoming waves, the multiple scattering approach has been applied. The latter is based on the superposition of the incident wave potential and various orders of propagating and evanescent modes that are scattered and radiated by the array members. The method of matched axisymmetric eigenfunction expansions and the multiple scattering approach have been thoroughly presented in [57–59], so they are no further elaborated here.

Having calculated the velocity potentials in all fluid regions, the time dependent volume flow $Q^q(r_q, \theta_q, z_q, t) = Re\{q^q(r_q, \theta_q, z_q)e^{-i\omega t}\}$, produced by the oscillating internal water surface in the q device, q =1,2,3, equals

$$q^q = \iint_{S_i^q} \frac{\partial \varphi^q}{\partial z} r_q dr_q d\theta_q, \tag{17}$$

where S_i^q is the cross sectional area of the inner water surface inside the OWC device q.

In our case, a Wells-type air turbine is assumed to be placed in each device's duct between the chamber and the outer atmosphere since it rotates in one direction regardless of the direction of the air flow. The pneumatic admittance of the air turbine is considered equal to the one by [60], i.e., $\Lambda^q = 343.848\ m^5/(kNs)$. For simplicity, the total volume flow q^q in the q device is proportional to the chamber air pressure [58]:

$$q^q = \Lambda^q \cdot p_0^q. \tag{18}$$

In Equation 18, the term Λ^q attains the same value regardless of the examined device q.

Finally, the absorbed power, P^q, of each q OWC device of the array, via Equation 18, can be written as [61]

$$P^q = \frac{1}{2} Re\left\{q^q \cdot \overline{p_0^q}\right\} = \frac{1}{2} \cdot \Lambda^q \cdot \left|p_0^q\right|^2. \tag{19}$$

3.2. Mooring system

In this section, the characteristics of the mooring system of the REFOS platform are determined. Initializing the procedure, it is necessary to decide the mooring system configuration, regarding the number of lines as well as their directions. In the present work, a catenary mooring system is selected for the REFOS structure. The system is assumed to consist of 3 lines, one attached to each inner concentric cylinder of each OWC device (see Figure 7). The fairlead coordinates as well as the line angles with respect to the global coordinate system (i.e., originating from the sea surface and the center of the central cylindrical body supporting the WT) are as follows.

Line 1: (x, y, z, α) = (−28.87 m, 0 m, −20 m, 180 deg)
Line 2: (x, y, z, α) = (14.43 m, 25 m, −20 m, 60 deg)
Line 3: (x, y, z, α) = (14.43 m, −25 m, −20 m, 300 deg)

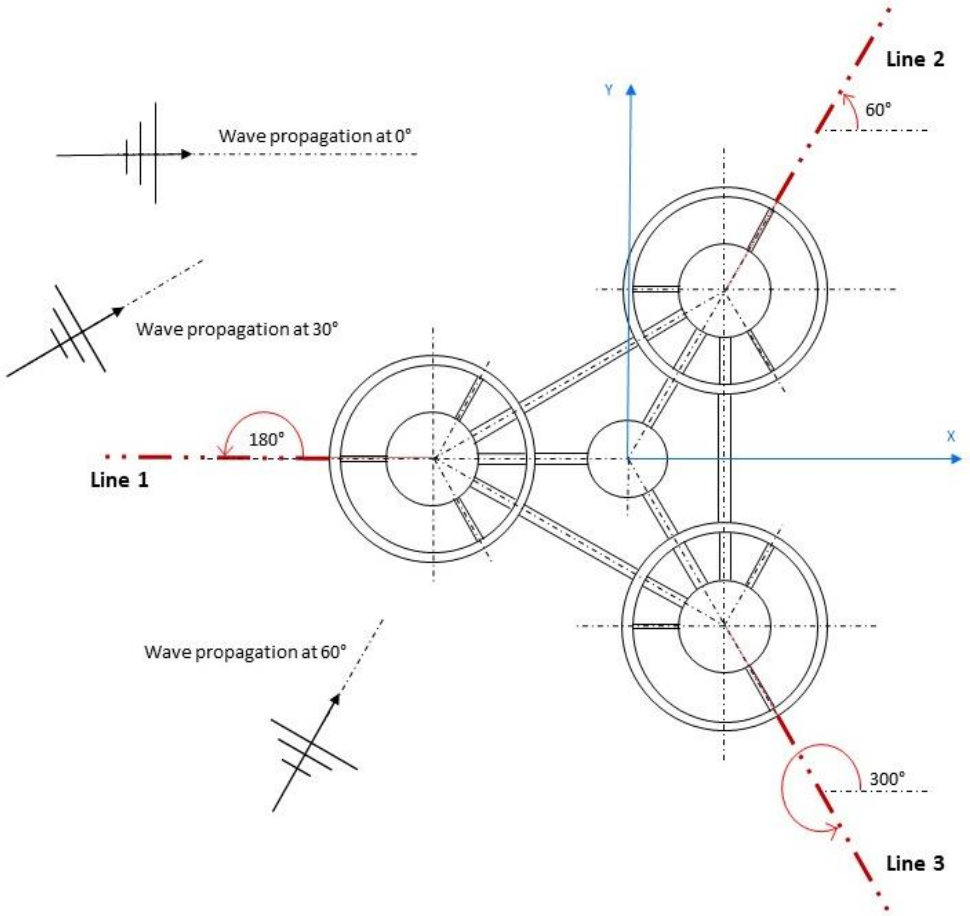

Figure 7. Schematic representation of the examined mooring system composed of three identical mooring lines.

In terms of materials, a studless chain of Class R3 is used for the mooring lines. The installation depth was considered the same with the TLP concept (about 200 m) for comparison purposes. Moreover, for the maximum offset criterion δx, it holds that $\delta x/D = 6\%$. Here, D stands for the distance of the fairlead from the seabed, i.e., $D = 180$ m. The line characteristics and the resulting horizontal pretension are shown in Table 10.

Table 10. Studless chain line specifications [62].

Diameter	0.127 m
Mass	323 kg/m
Weight in water	2913.89 N/m
Axial rigidity (EA)	1420 MN
Minimum Breaking Load (MBL)	12171 kN
Horizontal Pretension	2800 kN

Last but not least, the stiffness matrix with respect to the global coordinate system was estimated and is shown in Table 11.

Table 11. Total stiffness matrix (in [kN/m; kNm]) of the entire mooring system consisting of studless chains with respect to the global coordinate system.

230.801	0	0	0	−4616.010	0
0	7.250	0	144.992	0	−104.660
0	0	55.449	0	0.185	0
0	144.992	0	26003.586	0	−2093.199
−4616.010	0	0.185	0	115422.595	0
0	−104.660	0	−2093.199	0	52614.864

3.3. Coupled hydro-aero-elastic formulation

In order to investigate the dynamic equilibrium of the forces acting on the REFOS structure as well as to determine its total responses, the following system of differential equations of motion, describing the coupled hydro-aero-elastic problem in the frequency domain, was formulated, taking also into account the catenary mooring system that is applied instead of the TLP arrangement.

$$\sum_{j=1}^{6}\left[-\omega^2\left(M_{i,j}+M_{i,j}^{WT}+A_{i,j}+\frac{i}{\omega}B_{i,j}+\frac{i}{\omega}B_{i,j}^{WT}+\frac{i}{\omega}B_{i,j}^{m}\right)+C_{i,j}^{H}+C_{i,j}^{m}+C_{i,j}^{WT}\right]\Xi_{j0}-f_{P,i}^{T}=f_i^{T},\ \ i=1,\dots,6 \tag{20}$$

Here, $A_{i,j}$, $B_{i,j}$ are the hydrodynamic mass and potential damping coefficients of the platform [31]; f_i^T and $f_{P,i}^T$ are the exciting and the pressure hydrodynamic forces acting on the platform [31]; Ξ_{j0} is the motion component of the REFOS system in the *j-th* direction with respect to a global co-ordinate system; $M_{i,j}$ is the platform's mass matrix; $C_{i,j}^H$ is the platform's hydrostatic restoring stiffness matrix. Regarding the contribution of the wind turbine, the mass matrix $M_{i,j}^{WT}$ includes the WT inertia (including the gyroscopic effects due to rotation), the term $B_{i,j}^{WT}$ denotes the damping matrix that includes the WT damping due to rotation and aerodynamics, and finally, its stiffness matrix $C_{i,j}{}^{WT}$ includes the contributions from both aerodynamics and gravity [31]. The remaining terms $B_{i,j}{}^m$ and $C_{i,j}{}^m$ are the mooring system's damping matrix and restoring stiffness matrix, respectively, with respect to the global co-ordinate system as well. The reader is referred to [31–33] for analytical representations of the above coefficients, as well as for a detailed presentation of the coupled hydro-aero-elastic formulation.

4. Calculations and results

The hydrodynamic analysis of the REFOS components was conducted using the HAMVAB software [25,31,63]. The latter was preferred in the present contribution against other available numerical tools since, by keeping the same accuracy with them [64,65], it represents an efficient tool in the early design phases of such floating structures without requiring much RAM or computational time (i.e., central computational unit (CPU) time for each wave frequency is about 56 s). Setting the new data in the input files of the program along with all the respective specifications of the mooring lines, the analysis was performed in the frequency domain at a range of ω = [0.05, 3] rad/s with a step of 0.05 rad/s, as well as for three different wave directions, i.e., 0 deg, 30 deg and 60 deg, with respect to the global coordinate system (see Figure 7). For comparison purposes with the quasi-static analysis, a free-floating case was also investigated, whereas TLP case data were already available [31–33]. The motions of the floater can be expressed in terms of the response amplitude operator (RAO). The

dynamic modeling enables the evaluation of the dynamic tension at the top of each line and subsequently the mooring line damping and the mooring restoring coefficients. To perform such calculations demands an iterative procedure, where RAOs need to converge to some extent of precision, re-evaluating the dynamic tensions of the lines. From this, the mooring system's damping matrix and restoring stiffness matrix can be derived, consequently resulting in the sought-for matrices for each investigated frequency [66].

In Figures 8 and 9, all cases are compared referring to the three wave directions respectively. The figures display the RAOs of surge, heave and pitch motions and rotations, along with the pressure inside each OWC device. Regarding motion RAOs (see Figure 8), higher values in surge motion are depicted in the lower frequency range. Concerning the maximization of the surge RAO of the moored platform, this can be traced back to the mooring restoring stiffness, which imposes a resonance location in the surge motion at $\omega \approx 0.1$ rad/s. In the heave direction, the RAO motions of the free floating and moored with catenary lines structures start their variation from unity for ω tending to zero. However, this is not the case for the TLP case, since the appeared small responses are expected, as by definition the mooring system is more rigid. Catenary system responses are also shown to be close to the ones of the free-floating case, except for pitch motion, where the peak of the figure is shifted in lower values of ω. As far as the effect of the wave direction on the motions of the structure is concerned, it can be seen from the figures that the wave heading angle does not seem to affect the platform motions since the RAOs in the examined directions attain a similar variation pattern regardless the wave direction angle.

In Figure 9 the inner air pressure head of the three OWCs is presented for the examined wave heading angles. The results indicate that the angle of the wave train and the location of the OWC to the wave impact affect the values of $p_0^q, q = 1,2,3$. It is shown that higher pressure values are always developed in the windward OWCs; however, depending on the wave direction, equivalent results occur in the leeward ones. Furthermore, it can be seen that p_0^q attains a peculiar behavior at the neighborhood of $\omega \approx 0.8$ rad/s regardless of the wave direction angle, the examined device and the mooring type. This ω value corresponds to the frequency where the pumping resonance of the water column inside the oscillating chamber occurs. Also, the inner air pressure of the OWCs in the catenary mooring case attains a maximum at $\omega \approx 0.45$ rad/s. This can be traced back to the pitch motion of the structure, which maximizes also at the same wave frequency.

For investigating the dynamic effects, a spring and damping constant were required to perform the dynamic analysis of the mooring system. Regarding the examined frequencies, the range [0.95, 1.15] rad/s was investigated, as it corresponds to frequently observed sea-states. Table 12 presents the surge and heave responses (RAOs), $\Xi_{j0}, j = 1,3$, as well as the absorbed wave energy by the OWCs, $P^q, q = 1,2,3$. It can be observed that the heave responses (Heave) of the TLP hybrid structure attain the least values compared to the quasi-static and dynamic cases. Also, the absorbed wave energy (Eabs) from the TLP structure is higher than the corresponding values of the other two examined mooring cases, for ω = 0.95 rad/s and ω = 1 rad/s. On the other hand, the rest of the examined frequencies show increased P^q values that surpass the respective ones from the TLP case. This can be traced back to the dynamic effect of the moorings, which seems to be beneficial for the air pressure head inside the OWCs, and consequently to the absorbed wave power.

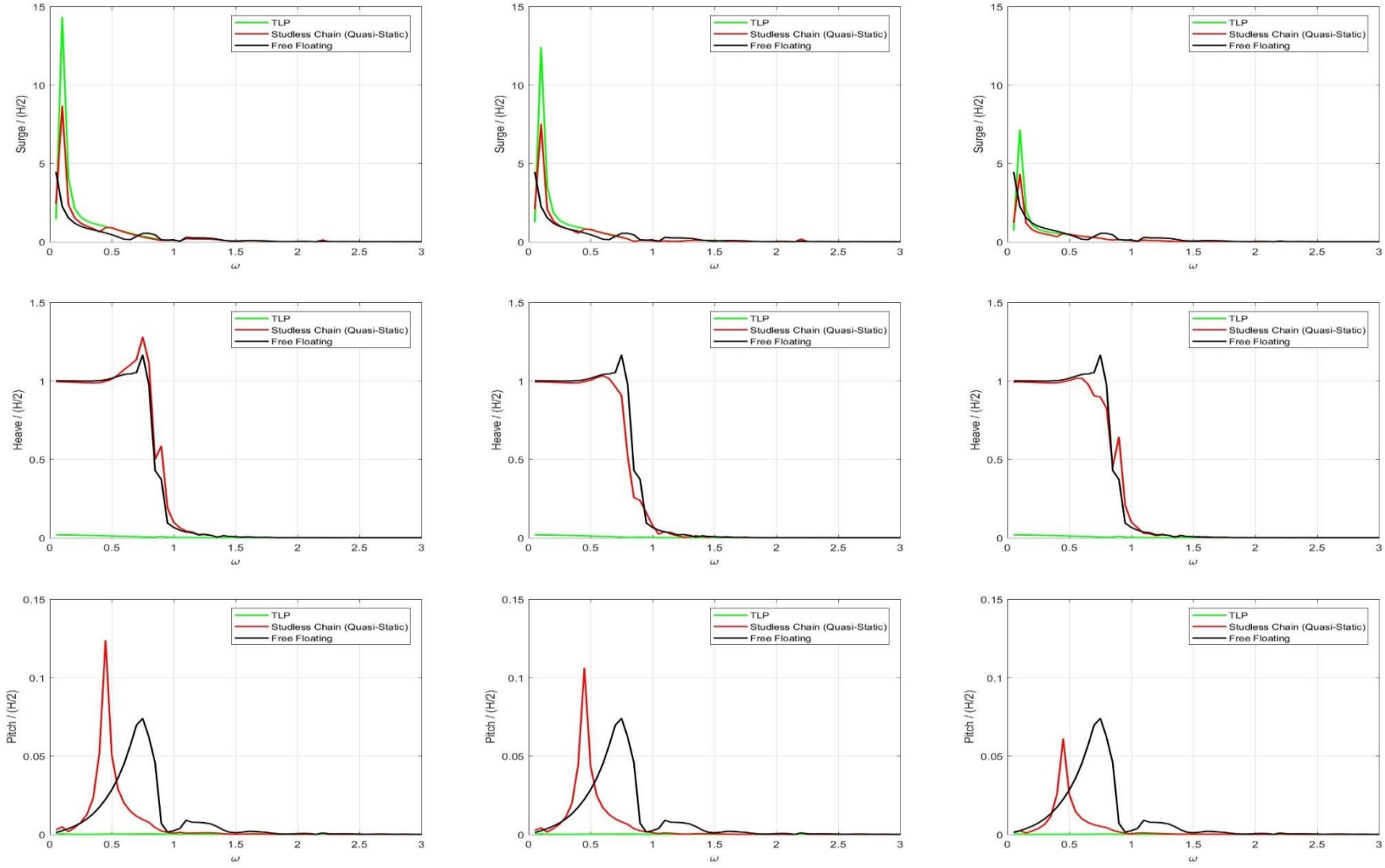

Figure 8. Platform's Surge, Heave and Pitch RAOs motions comparing the cases of TLP, free-floating and studless chain catenaries excited by different wave angles: (a) wave of 0 deg direction, (b) wave of 30 deg direction, (c) wave of 60 deg direction.

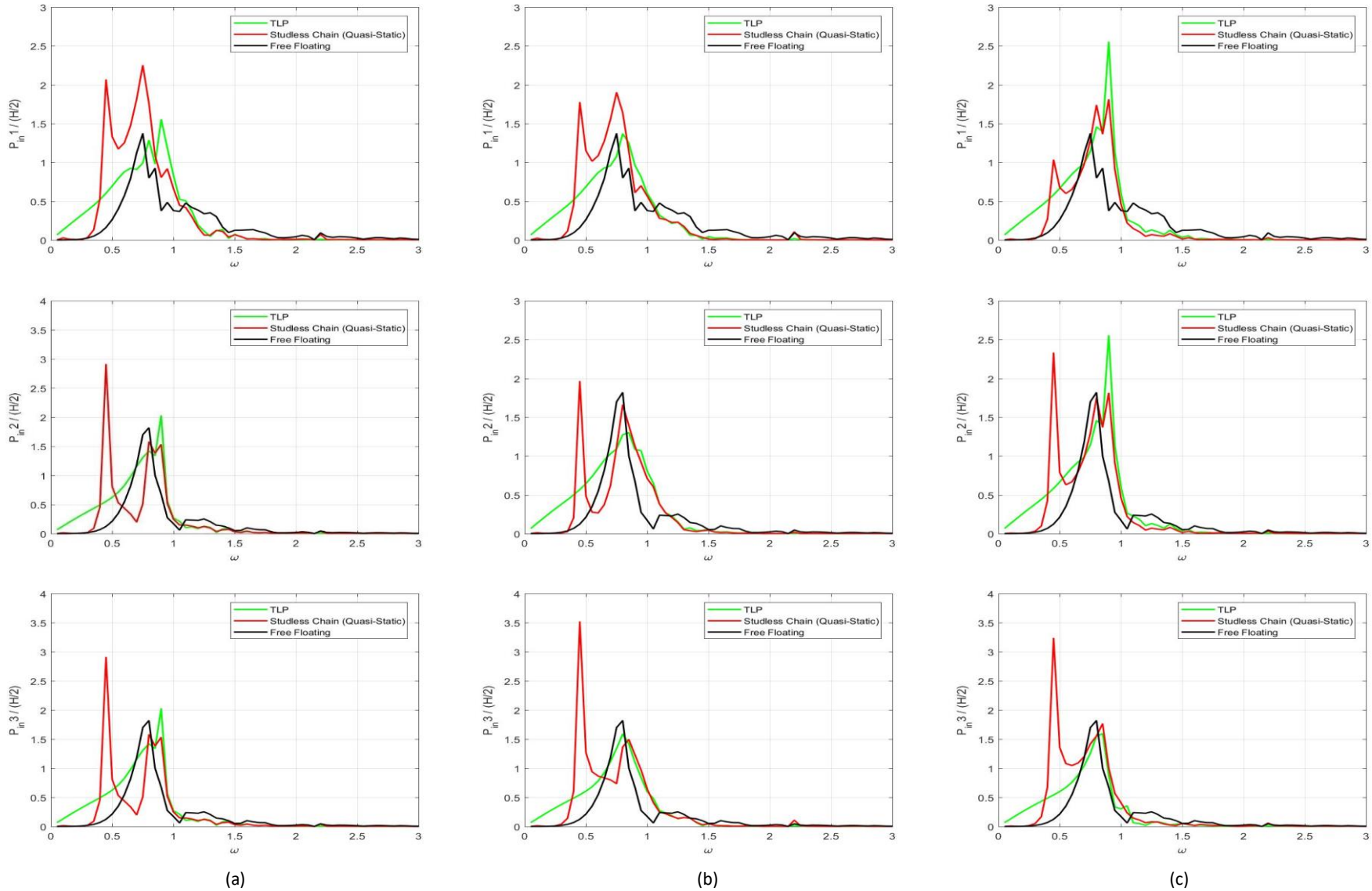

Figure 9. Air pressure head inside the OWC chambers comparing the cases of TLP, free-floating and studless chain catenaries excited by different wave angles: (a) wave of 0 deg direction, (b) wave of 30 deg direction, (c) wave of 60 deg direction.

Table 12. Dimensionless data results for the dynamic analysis (Dyn) and comparison with the respective data from the TLP case and the quasi-static (QS) approach.

		ω (rad/s)				
		0.95	1.00	1.05	1.10	1.15
Surge	*TLP*	0.1147	0.1225	0.0375	0.2284	0.2124
	Chain QS	0.0884	0.0992	0.0311	0.1976	0.1828
	Chain Dyn	0.0922	0.0925	0.0257	0.2048	0.1857
Heave	*TLP*	0.0026	0.0016	0.0013	0.0010	0.0010
	Chain QS	0.1889	0.0985	0.0630	0.0424	0.0357
	Chain Dyn	0.0582	0.0393	0.0327	0.0286	0.0317
Eabs	*TLP*	0.1533	0.0600	0.0247	0.0179	0.0103
	Chain QS	0.1036	0.0401	0.0165	0.0142	0.0077
	Chain Dyn	0.1240	0.0508	0.0304	0.0247	0.0166

5. Energy output estimation

In this section, the amount of the offshore wind and wave energy produced via the discussed multi-purpose platform will be estimated, comparing also the alternative mooring systems in terms of efficiency. During its operational phase, the installed wind turbine, i.e., the DTU 10 MW RWT, will be producing energy continuously except for the maintenance periods and during the hours with wind conditions outside the operating range. Offshore sites are characterized by strong and steady wind regime, so a high energy output is anticipated. The power curve of the DTU 10MW RWT as well as the rest of the specifications can be found in [67]. The cut-in—cut-out range is [4,25] m/s, and the rated speed is 11.4 m/s, while the manufacturer states that the rated power is 10640 kW.

As far as wave energy converters are concerned, it is necessary to evaluate the produced energy depending on the installation site sea-state conditions. From a mathematical scope, a simple approximate analytical solution has been derived for the efficiency of wave energy absorption of an OWC wave energy device [68]. However, since moored structures are discussed in this work, the influence of the mooring system cannot be neglected, as it affects the structure's responses. Such work, comparing a TLP and a catenary mooring system towards the OWC's efficiency, has proven the former as the most efficient case in the entire band of the examined wave frequencies [69]. Although the benefits of this higher efficiency are very important, they are mitigated due to the high construction and installation costs of the TLP moorings, which set the motivation for further investigation on more economic solutions.

5.1. Offshore wind energy

As already mentioned, the produced energy will be calculated regarding the three examined locations mentioned in Section 2. However, the wind speed timeseries refer to 100 m asl, while the hub height of the DTU 10 MW RWT is 119 m. Thus, the data were adjusted accordingly given that

$$u_{h_2} = u_{h_1} \frac{\ln\left(\frac{h_2}{z_0}\right)}{\ln\left(\frac{h_1}{z_0}\right)}, \tag{21}$$

where u_{h_2} (m/s) is the calculated wind speed at height h_2 (m), u_{h_1} (m/s) is the known wind speed at height h_1 (m), and z_0 (m) is the roughness length equal to 0.0002 m for neutral atmospheric conditions.

The mean annual energy as well as the monthly mean energy can be estimated, analyzing the 20-year datasets. For the former one, each year is analyzed separately, while for the latter, a monthly clustering is needed. Lastly, due to the fact that the timeseries are in 1-hour timesteps, the sum of the power values that correspond to the wind speed data based on the power curve will result in the sought-for energy. The results are shown in Figures 10 and 11. Regarding the three locations, the annual energy output is relatively higher in locations L1 and L3 than in location L2, while the same feature is observed in the summer period at the respective monthly mean values (6.5–7 GWh on average in July and August). The exact opposite phenomenon can be seen to occur in the winter period, yet at a much lower intensity. The aforementioned observations verify and prove the presence of the strong Etesian winds in the Aegean Sea, which mostly affect locations L1 and L3 in our case. As far as energy output is concerned, these locations produce 56.30 GWh/y and 58.55 GWh/y on average, respectively, while for L2 the production is limited to 46.70 GWh/y. In general, seasonal periodicity is clearly shown in the monthly results, while similar conclusions for inter-annual cycles require longer datasets. Moreover, the capacity factor (CF) is calculated for every site and year (Figure 12). The capacity factor is the ratio of the actual energy produced in a given period to the hypothetical maximum possible, i.e., full time operation of the WT at the rated power. In our case, full time at rated power equals 365 d × 24 h × 10640 kW = 93206400 kWh/y, and the results correspond to the produced energy depicted in Figure 10. Regarding the discussed locations, L1 and L3 appear to be really promising sites with CFs of 60.4% and 62.8% on average, respectively, while L2 is also a very reliable choice, with a CF of 50.1%. Such CF values are relatively much higher than the ones that appear in a typical onshore project, yet in these sites there is a very high frequency of occurrence of wind speeds in the operational WT range of [4,25] m/s (86.5% for L1, 81.3% for L2 and 87.5% for L3). Consequently, the intense wind climate in these offshore locations may render such projects reliable and promising for financially feasible production of green energy.

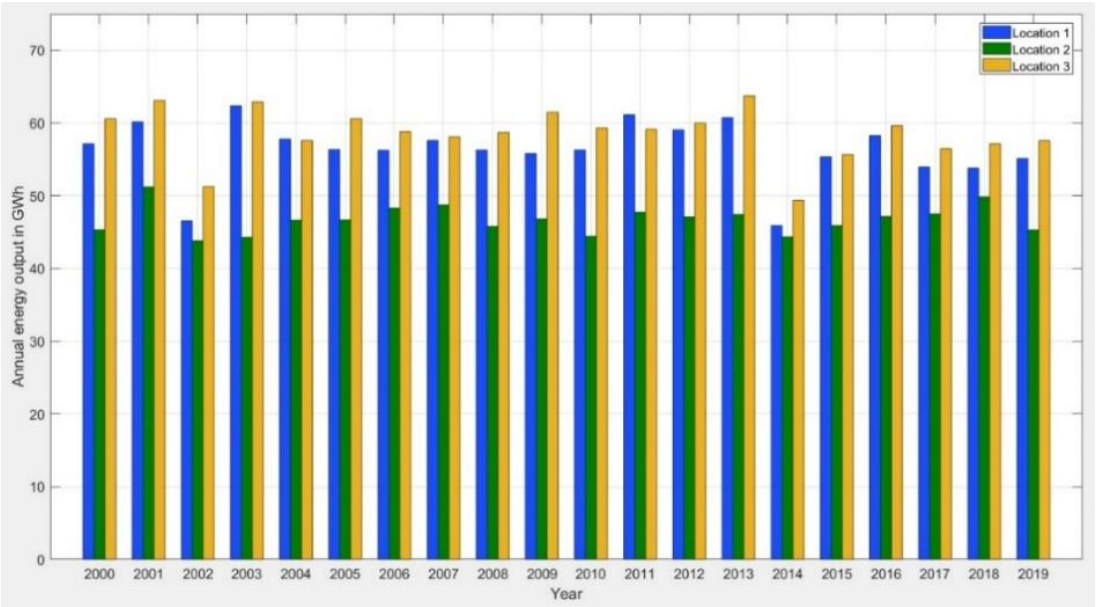

Figure 10. Annual energy output in GWh for the three examined locations (L1 in blue, L2 in green, L3 in orange) from 2000 until 2019 (20-year datasets).

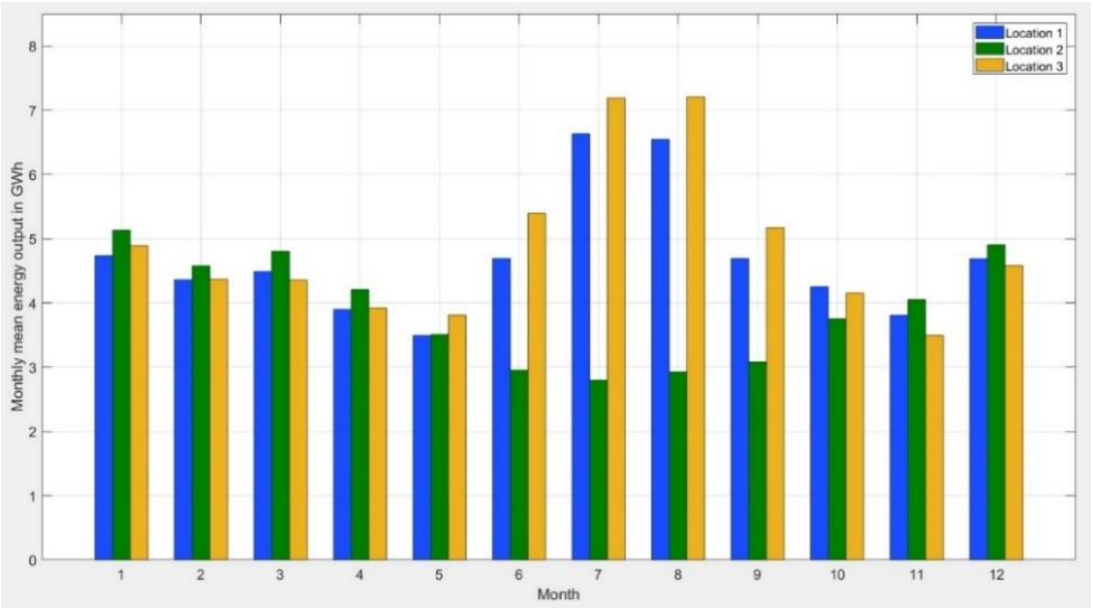

Figure 11. Monthly mean energy output in GWh for the three examined locations (L1 in blue, L2 in green, L3 in orange) based on 20-year datasets.

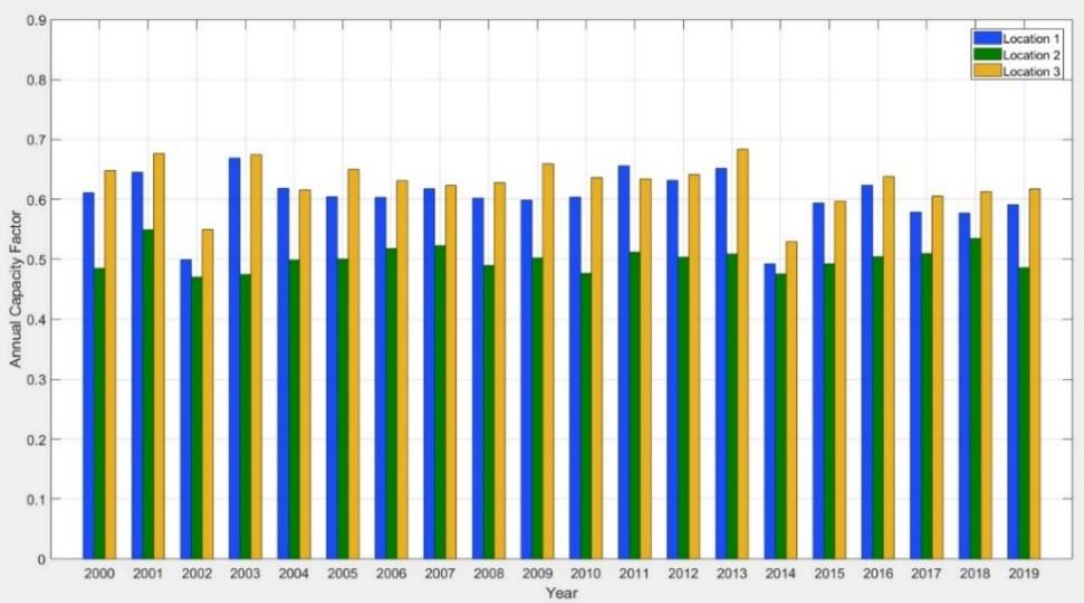

Figure 12. Annual capacity factor for the three examined locations (L1 in blue, L2 in green, L3 in orange) from 2000 until 2019 (20-year datasets).

5.2. Wave energy

Installing the REFOS platform at the investigated installation sites, OWC devices will produce energy depending on the wave climate and the structure's responses. In order to estimate the absorbed energy from the devices, the JONSWAP spectrum, provided by DNV [70], and absorbed energy results, P^q, for each device should be utilized. Regarding the JONSWAP spectrum, $S_J(\omega)$, which corresponds to developing sea-states in fetch limited situations, it is formulated via the Pierson-Moskowitz spectrum that describes fully developed seas. Subsequently, the absorbed power per sea-state (spectrum) can be calculated via Equation 22. At this stage, the results are independent of location yet depend on the mooring system and wave direction:

$$P = \int 2\, P^q\, S_J(\omega)\, d\omega, \tag{22}$$

where P^q is defined in Equation (19).

The absorbed energy per sea-state is estimated by multiplying the tables of sea-state occurrences with the ones of the absorbed power and by dividing all the cell values with the 20 years of the examined data, in order to derive the mean annual absorbed energy per sea-state, per location and for each mooring system case. By adding all cell values, the total mean annual wave energy absorbed from the OWC devices is calculated for every case, and the final results are presented in Table 13. Clearly, location L2, which is characterized by the greater fetch lengths and sea-state conditions, has the highest wave energy production. Comparing the other two installation sites, location L3 exhibits the lowest wave energy, due to the topography of the area. As far as the mooring system is concerned, the TLP design is characterized by the highest efficiency, as it is by definition the most rigid solution. However, the catenary mooring system also presents high energy production. Comparing all cases in terms of the wave direction, peak values appear when the excitation wave propagates at 60 deg, while the opposite is observed for the 30 deg wave.

Table 13. Total mean annual absorbed energy in MWh/y for every examined mooring system, wave direction and location.

Moorings	Wave direction	*Location L1*	*Location L2*	*Location L3*
TLP	0 deg	332.53	608.33	317.81
	30 deg	244.71	463.93	233.88
	60 deg	402.28	722.35	384.42
Chain	0 deg	257.89	518.79	246.33
	30 deg	251.70	496.22	240.37
	60 deg	309.54	606.75	295.45

Table 14. Annual absorbed energy in kWh/y for 0 deg wave direction regarding every location and comparing the TLP case with the two analysis approaches of the examined chain mooring system: quasi-static (QS) and dynamic (Dyn). Highest values in every case are depicted in bold.

Cases		Peak Wave Period	Significant Wave Height H_s (m)					
		T_p (s)	0−1	1−2	2−3	3−4	4−5	5−6
L1	*TLP*	5−6	1227	56732	3213	0	0	0
		6−7	61	15497	**145020**	4935	0	0
	QS	5−6	829	38508	2216	0	0	0
		6−7	49	12393	**103460**	3334	0	0
	Dyn	5−6	470	24691	1864	0	0	0
		6−7	52	13073	**105050**	3380	0	0
L2	*TLP*	5−6	4263	44370	1257	0	0	0
		6−7	2018	71843	**119730**	2263	0	0
	QS	5−6	2880	30117	867	0	0	0
		6−7	1614	57454	**85411**	1529	0	0
	Dyn	5−6	1633	19311	729	0	0	0
		6−7	1703	60604	**86723**	1550	0	0
L3	*TLP*	5−6	4931	67585	98	0	0	0
		6−7	1100	64675	**91490**	314	0	0
	QS	5−6	3331	45875	67	0	0	0
		6−7	879	51722	**65268**	212	0	0
	Dyn	5−6	1888	29414	57	0	0	0
		6−7	928	54558	**66270**	215	0	0

As far as the results of the dynamic analysis are concerned, wave energy calculations were performed regarding two wave frequencies: ω = 0.95 rad/s and ω = 1.15 rad/s. These correspond to the [6,7] (s) and [5,6] (s) peak wave period classes, respectively. The latter classes are characterized by rather high frequency of occurrences based on the analysis in Section 2.2. Table 14 presents the results from the dynamic analysis along with the respective ones from TLP and quasi-static approach for comparison purposes. It is observed that peak values of the wave energy for the TLP case attain higher values regardless of the examined location and the investigated sea-states. However, for a more comprehensive overview of the produced wave energy, dynamic results of every frequency are necessary to yield the complete power tables for every installation site.

6. Conclusions and discussion

Offshore wind is characterized as the main medium for generating green energy in the near future [1]. The integration of technologies to exploit ocean wave energy potential is also in the spotlight for more effective offshore power plants. In this work, a multi-purpose hybrid (wind and wave energy) floating platform with two different mooring systems has been assessed at three locations of the Greek Seas. In this respect, the environmental conditions of the examined areas have been analyzed along with an extreme value analysis of the wind and sea states based on the Peak over Threshold method. The respective results were accounted for in the catenary mooring line system specification, which was also investigated in terms of power efficiency, performing both quasi-static and dynamic analyses. Dominant regarding the energy potential and preferred among others due to bathymetry, the selected locations were evaluated through their offshore wind and wave energy potential output.

In the frame of the POT method, it is shown that higher threshold selection than the one suggested from theory gave improved results based on the relevant diagnostic plots. All selections did not negate variance prerequisites and supported the bias-variance trade-off. Moreover, regarding return levels, the lowest wave design values correspond to location L3, while the highest wind speed design values were provided for location L1, due to the strong winter and summer (Etesian) winds as well as the lack of near highland. As far as the ultimate limit state analysis is concerned, the results of EVA were not critical for the floating system. The maximum 100-year return values of the examined variables were around 30 m/s and 7 m for wind speed and significant wave height, respectively, at L1 and 12.5 s for peak wave period at L2. Assuming an extreme sea-state of $[H_s–T_p]$ = [7–12.5], the structure did not show any cause for concern.

Concerning the energy output, higher offshore wind energy is capable of being produced in locations L1 and L3, due to the strong wind climate all year round. Location L2 is also a very promising site and showed a relatively high capacity factor, yet it presented the highest wave energy production, due to the greater fetch and swells that characterize the area. Regarding wave direction, the 60 deg wave gave the highest wave energy outputs overall, while the lowest results were derived from the wave propagating at 30 deg. Comparing the two main mooring systems in terms of efficiency, TLP represents the best-case scenario. Expected results were also determined with regard to the quasi-static and dynamic analyses. The dynamic approach presented higher peak wave energy production in the respective investigated sea-states. However, all frequency results are necessary to yield the complete power tables for every installation site and gain a more comprehensive overview of the energy status.

Considering all of the aforementioned facts regarding the research conducted for the purpose of this work, it can be concluded that catenary mooring systems are a very competitive solution for multi-purpose floating structures and floating wind turbines in general. Their performance in station-keeping as well as in ultimate limit states promises a reliable and robust design along with construction and installation financial feasibility. Such projects can become profitable, taking into account the decreased overall costs that lead to a lower levelized cost of energy (LCOE). Catenary mooring systems should also be studied regarding the dynamic responses of the lines, especially integrating more phenomena in the models such as vortex-induced vibrations (VIVs), seabed interactions and internal damping due to friction between the chain links, as well as avoiding snap loads and fatigue. The additional effects of mooring induced damping further decrease motions, which is expected to increase the efficiency of the OWCs. Further assessments, such as those described in Duan *et al.* [71] and Russo *et al.* [72], should also be performed regarding the offshore wind turbine performance, as applied coupled motions tilt the rotor and alter the turbine's operation. Moreover, fatigue analyses and anchor design should be

applied as well, while optimization of the air turbines of the OWCs would further contribute to making multi-purpose floating structures competitive in the energy market for offshore wind and wave co-exploitation.

Author contributions

Conceptualization, T.H.S. and D.N.K.; methodology, T.H.S. and D.N.K.; software, K.K.; validation, K.K.; formal analysis, T.H.S., D.N.K. and K.K.; investigation, K.K.; writing—original draft preparation, K.K.; writing—review and editing, T.H.S., D.N.K. and K.K. All authors have read and agreed to the published version of the manuscript.

Data availability statement

The ERA5 reanalysis dataset has been obtained from https://cds.climate.copernicus.eu (accessed on 3 March 2021).

Acknowledgments

The authors wish to express their appreciation to Professor Emeritus Spyridon Mavrakos, coordinator of the REFOS project [73], who provided the required data for the TLP moored floating structure.

Conflicts of interest

The authors declare no conflict of interest.

References

1. GWEC (2021) Global offshore wind report. Available from: https://gwec.net/global-offshore-wind-report-2021/.
2. Butterfield S, Musial W, Jonkman J, et al. (2007) Engineering challenges for floating offshore wind turbines. National Renewable Energy Laboratory, Golden, United States. Available from: https://www.nrel.gov/docs/fy07osti/38776.pdf.
3. Huijs F, de Ridder EJ, Savenije F (2014) Comparison of model tests and coupled simulations for a semi-submersible floating wind turbine. *Int Conf Offshore Mech Arct Eng* 45530: V09AT09A012. https://doi.org/10.1115/OMAE2014-23217
4. Roddier D, Cermelli C, Aubault A, et al. (2010) Windfloat: A floating foundation for offshore wind turbines. *J Renewable Sustainable Energy* 2: 033104. https://doi.org/10.1063/1.3435339
5. Borg M, Walkusch Jensen M, Urquhart S, et al. (2020) Technical definition of the tetraspar demonstrator floating wind turbine foundation. *Energies* 13: 4911. https://doi.org/10.3390/en13184911
6. Galvan J, Sánchez-Lara MJ, Mendikoa I, et al. (2018) NAUTILUS-DTU10 MW Floating Offshore Wind Turbine at Gulf of Maine: Public numerical models of an actively ballasted semisubmersible. *J Phy Conf Ser* 1102: 012015. https://doi.org/10.1088/1742-6596/1102/1/012015

7. Robertson A, Jonkman J, Masciola M, et al. (2014) Definition of the semisubmersible floating system for phase II of OC4. National Renewable Energy Laboratory, Golden, United States. Available from: https://www.nrel.gov/docs/fy14osti/60601.pdf.
8. Robertson AN, Wendt F, Jonkman JM, et al. (2017) OC5 project phase II: validation of global loads of the deepcwind floating semisubmersible wind turbine. *Energy Procedia* 137: 38–57. https://doi.org/10.1016/j.egypro.2017.10.333
9. Uzunoglu E, Karmakar D, Guedes Soares C (2016) Floating offshore wind platforms, *Floating offshore wind farms*, Springer, 53–76. https://doi.org/10.1007/978-3-319-27972-5_4
10. Pelagic Power AS (2010) Mobilising the total offshore renewable energy resource. Available from: www.pelagicpower.no.
11. Marine Power Systems. Available from: https://www.marinepowersystems.co.uk/dualsub/.
12. Floating Power Plant (FPP). Available from: http://www.floatingpowerplant.com/.
13. Bachynski EE, Moan T (2013) Point absorber design for a combined wind and wave energy converter on a tension-leg support structure. *Int Conf Offshore Mech Arct Eng* 55423: V008T09A025. https://doi.org/10.1115/OMAE2013-10429
14. Muliawan MJ, Karimirad M, Gao Z, et al. (2013) Extreme responses of a combined spar-type floating wind turbine and floating wave energy converter (STC) system with survival modes. Ocean Eng 65: 71–82. https://doi.org/10.1016/j.oceaneng.2013.03.002
15. Muliawan MJ, Karimirad M, Moan T (2013) Dynamic response and power performance of a combined spar-type floating wind turbine and coaxial floating wave energy converter. *Renewable Energy* 50: 47–57. https://doi.org/10.1016/j.renene.2012.05.025
16. Veigas M, Iglesias G (2015) A hybrid wave-wind offshore farm for an island. *International J Green Energy* 12: 570–576. https://doi.org/10.1080/15435075.2013.871724
17. Michailides C, Gao Z, Moan T (2016) Experimental and numerical study of the response of the offshore combined wind/wave energy concept SFC in extreme environmental conditions. *Mar Struct* 50: 35–54. https://doi.org/10.1016/j.marstruc.2016.06.005
18. Michailides C, Gao Z, Moan T (2016) Experimental study of the functionality of a semisubmersible wind turbine combined with flap-type Wave Energy Converters. *Renewable Energy* 93: 675–690. https://doi.org/10.1016/j.renene.2016.03.024
19. Gao Z, Moan T, Wan L, et al. (2016) Comparative numerical and experimental study of two combined wind and wave energy concepts. *J Ocean Eng Sci* 1: 36–51. https://doi.org/10.1016/j.joes.2015.12.006
20. Karimirad M, Koushan K (2016) WindWEC: Combining wind and wave energy inspired by hywind and wavestar. *2016 IEEE Int Conf Renewable Energy Res Appl*, 96–101. https://doi.org/10.1109/ICRERA.2016.7884433
21. Wang Y, Zhang L, Michailides C, et al. (2020) Hydrodynamic Response of a Combined Wind-Wave Marine Energy Structure. *J Mar Sci Eng* 8: 253. https://doi.org/10.3390/jmse8040253
22. Wang B, Deng Z, Zhang B (2022) Simulation of a novel wind–wave hybrid power generation system with hydraulic transmission. *Energy* 238: 121833. https://doi.org/10.1016/j.energy.2021.121833
23. Aubault A, Alves M, Sarmento A, et al. (2011) Modeling of an oscillating water column on the floating foundation WINDFLOAT. *Int Conf Ocean Offshore Arct Eng*, 235–246. https://doi.org/10.1115/OMAE2011-49014
24. Mazarakos T, Konispoliatis D, Manolas D, et al. (2015) Modelling of an offshore multi-purpose floating structure supporting a wind turbine including second-order wave loads. *11th Eur Wave Tidal Energy Conf*, 7–10.

25. Mazarakos T, Konispoliatis D, Katsaounis G, et al. (2019) Numerical and experimental studies of a multi-purpose floating TLP structure for combined wind and wave energy exploitation. *Mediterr Mar Sci* 20: 745–763. https://doi.org/10.12681/mms.19366
26. Perez-Collazo C, Greaves D, Iglesias G (2018) A novel hybrid wind-wave energy converter for jacket-frame substructures. *Energies* 11: 637. https://doi.org/10.3390/en11030637
27. Perez-Collazo C, Pemberton R, Greaves D, et al. (2019) Monopile-mounted wave energy converter for a hybrid wind-wave system. *Energy Conversion and Management* 199: 111971. https://doi.org/10.1016/j.enconman.2019.111971
28. Sarmiento J, Iturrioz A, Ayllón V, et al. (2019) Experimental modelling of a multi-use floating platform for wave and wind energy harvesting. *Ocean Eng* 173: 761–773. https://doi.org/10.1016/j.oceaneng.2018.12.046
29. Michele S, Renzi E, Perez-Collazo C, et al. (2019) Power extraction in regular and random waves from an OWC in hybrid wind-wave energy systems. *Ocean Eng* 191: 106519. https://doi.org/10.1016/j.oceaneng.2019.106519
30. Zhou Y, Ning D, Shi W, et al. (2020) Hydrodynamic investigation on an OWC wave energy converter integrated into an offshore wind turbine monopile. *Coast Eng* 162: 103731. https://doi.org/10.1016/j.coastaleng.2020.103731
31. Konispoliatis DN, Katsaounis GM, Manolas DI, et al. (2021) REFOS: A Renewable Energy Multi-Purpose Floating Offshore System. *Energies* 14: 3126. https://doi.org/10.3390/en14113126
32. Konispoliatis D, Mazarakos T, Soukissian T, et al. (2018) REFOS: A multi-purpose floating platform suitable for wind and wave energy exploitation. *Proc 11th Int Conf Deregulated Electr Mark Issues South East Eur*, 20–21.
33. Konispoliatis DN, Manolas DI, Voutsinas SG, et al. (2022) Coupled Dynamic Response of an Offshore Multi-Purpose Floating Structure Suitable for Wind and Wave Energy Exploitation. *Front Energy Res* 10: 920151.
34. Esteban MD, Diez JJ, López JS, et al. (2011) Why offshore wind energy? *Renewable Energy* 36: 444–450. https://doi.org/10.1016/j.renene.2010.07.009
35. Martinez A, Iglesias G (2021) Multi-parameter analysis and mapping of the levelised cost of energy from floating offshore wind in the Mediterranean Sea. *Energy Convers Manage* 243: 114416. https://doi.org/10.1016/j.enconman.2021.114416
36. Soukissian T, Papadopoulos A, Skrimizeas P, et al. (2017) Assessment of offshore wind power potential in the Aegean and Ionian Seas based on high-resolution hindcast model results. *AIMS Energy* 5: 268–289. https://doi.org/10.3934/energy.2017.2.268
37. Kardakaris K, Boufidi I, Soukissian T (2021) Offshore wind and wave energy complementarity in the Greek seas based on ERA5 data. *Atmosphere* 12: 1360. https://doi.org/10.3390/atmos12101360
38. EMODnet Bathymetry. Available from: https://portal.emodnet-bathymetry.eu/.
39. Hersbach H, Bell B, Berrisford P, et al. (2020) The ERA5 global reanalysis. *QJR Meteorol Soc* 146: 1999–2049. https://doi.org/10.1002/qj.3803
40. Farjami H, Hesari ARE (2020) Assessment of sea surface wind field pattern over the Caspian Sea using EOF analysis. *Reg Stud Mar Sci* 35: 101254. https://doi.org/10.1016/j.rsma.2020.101254
41. de Assis Tavares LF, Shadman M, de Freitas Assad LP, et al. (2020) Assessment of the offshore wind technical potential for the Brazilian Southeast and South regions. *Energy* 196: 117097. https://doi.org/10.1016/j.energy.2020.117097
42. Bruno MF, Molfetta MG, Totaro V, et al. (2020) Performance assessment of ERA5 wave data in a swell dominated region. *J Mar Sci Eng* 8: 214. https://doi.org/10.3390/jmse8030214

43. Karathanasi FE, Soukissian TH, Hayes DR (2022) Wave Analysis for Offshore Aquaculture Projects: A Case Study for the Eastern Mediterranean Sea. *Climate* 10: 2 https://doi.org/10.3390/cli10010002
44. Soukissian TH, Tsalis C (2015) The effect of the generalized extreme value distribution parameter estimation methods in extreme wind speed prediction. *Nat Hazards* 78: 1777–1809. https://doi.org/10.1007/s11069-015-1800-0
45. Soukissian TH, Tsalis C (2018) Effects of parameter estimation method and sample size in metocean design conditions. *Ocean Eng* 169: 19–37. https://doi.org/10.1016/j.oceaneng.2018.09.017
46. Soukissian TH, Kalantzi GD (2006) Extreme value analysis methods used for extreme wave prediction. *Sixteenth Int Offshore Polar Eng Conf*. OnePetro.
47. Sartini L, Mentaschi L, Besio G (2015) Comparing different extreme wave analysis models for wave climate assessment along the Italian coast. *Coastal Eng* 100: 37–47. https://doi.org/10.1016/j.coastaleng.2015.03.006
48. Park SB, Shin SY, Jung KH, et al. (2020) Extreme Value Analysis of Metocean Data for Barents Sea. *J Ocean Eng Technol* 34: 26–36. https://doi.org/10.26748/KSOE.2019.094
49. Devis-Morales A, Montoya-Sánchez RA, Bernal G, et al. (2017) Assessment of extreme wind and waves in the Colombian Caribbean Sea for offshore applications. *Appl Ocean Res* 69: 10–26. https://doi.org/10.1016/j.apor.2017.09.012
50. Ferreira JA, Guedes Soares C (1998) An application of the peaks over threshold method to predict extremes of significant wave height. *J Offshore Mech Arct Eng* 120: 165–176. https://doi.org/10.1115/1.2829537
51. Caires S, Sterl A (2005) 100-year return value estimates for ocean wind speed and significant wave height from the ERA-40 data. *J Clim* 18: 1032–1048. https://doi.org/10.1175/JCLI-3312.1
52. Méndez FJ, Menéndez M, Luceño A, et al. (2006) Estimation of the long-term variability of extreme significant wave height using a time-dependent peak over threshold (pot) model. *J Geophys Res Oceans* 111.
53. Dissanayake P, Flock T, Meier J, et al. (2021) Modelling short-and long-term dependencies of clustered high-threshold exceedances in significant wave heights. *Mathematics* 9: 2817. https://doi.org/10.3390/math9212817
54. Coles S (2001) *An Introduction to Statistical Modeling of Extreme Values*. Bristol, UK. Springer.
55. Lemos IP, Lima AMG, Duarte MAV (2020) thresholdmodeling: A Python package for modeling excesses over a threshold using the Peak-Over-Threshold Method and the Generalized Pareto Distribution. *J Open Source Software* 5: 2013. https://doi.org/10.21105/joss.02013
56. Bak C, Zahle F, Bitsche R, et. al. (2013) The DTU 10-MW reference wind turbine. *Dan Wind Power Res 2013.*
57. Konispoliatis D, Mazarakos T, Mavrakos S (2016) Hydrodynamic analysis of three-unit arrays of floating annular oscillating-water column wave energy converters. *Appl Ocean Res* 61: 42–64. https://doi.org/10.1016/j.apor.2016.10.003
58. Mavrakos SA, Koumoutsakos P (1987) Hydrodynamic interaction among vertical axisymmetric bodies restrained in waves. *Appl Ocean Res* 9: 128–140. https://doi.org/10.1016/0141-1187(87)90017-4
59. Mavrakos S (1991) Hydrodynamic coefficients for groups of interacting vertical axisymmetric bodies. *Ocean Eng* 18: 485–515. https://doi.org/10.1016/0029-8018(91)90027-N

60. Konispoliatis D, Mazarakos T, Katsidoniotaki E, et al. (2019) Efficiency of an array of OWC devices equipped with air turbines with pitch control. *Proc 13th Eur Wave Tidal Energy Conf*, Napoli, Italy, 1–6.
61. Falnes J (2002) *Ocean Waves and Oscillating Systems*. Cambridge University Press: Cambridge, UK; New York, NY, USA.
62. Anchor Marine & Industrial Supply Inc. Available from: https://anchormarinehouston.com/chain/
63. Mavrakos S (1995) User's Manual for the Software HAMVAB. *School of Naval Architecture and Marine Engineering, Laboratory for Floating Structures and Mooring Systems*, Athens, Greece.
64. Mavrakos SA, McIver P (1997) Comparison of methods for computing hydrodynamic characteristics of arrays of wave power devices. *Appl Ocean Res* 19: 283–291. https://doi.org/10.1016/S0141-1187(97)00029-1
65. Konispoliatis DN, Mavrakos SA (2016) Hydrodynamic analysis of an array of interacting free-floating oscillating water column (OWC's) devices. *Ocean Eng* 111: 179–197. https://doi.org/10.1016/j.oceaneng.2015.10.034 Get righ
66. Konispoliatis DN, Chatjigeorgiou IK, Mavrakos SA (2022) Hydrodynamics of a Moored Permeable Vertical Cylindrical Body. *J Mar Sci Eng* 10: 403. https://doi.org/10.3390/jmse10030403
67. NREL DTU 10 MW. Available from: https://nrel.github.io/turbine-models/DTU_10MW_178_RWT_v1.html.
68. Evans D V (1978) The oscillating water column wave-energy device. *IMA J Appl Math* 22: 423–433.
69. Konispoliatis DN, Mavrakos AS, Mavrakos SA (2020) Efficiency of an oscillating water column device for several mooring systems. *Developments in Renewable Energies Offshor*, CRC Press. 666–673.
70. DNV GL Class Guideline: DNVGL-CG-0130. Wave Loads. Available from: https://studylib.net/doc/25365327/dnvgl-cg-0130.
71. Duan F, Hu Z, Niedzwecki JM (2016) Model test investigation of a spar floating wind turbine. *Mar Struct* 49: 76–96. https://doi.org/10.1016/j.marstruc.2016.05.011
72. Russo S, Contestabile P, Bardazzi A, et al. (2021) Dynamic loads and response of a spar buoy wind turbine with pitch-controlled rotating blades: An experimental study. *Energies* 14: 3598. https://doi.org/10.3390/en14123598
73. Life-Cycle Assessment of a Renewable Energy Multi-Purpose Floating Offshore System, REFOS (709526) project. EU Framework Program for Research and Innovation, Research Fund for Coal and Steel. Available from: www.refos-project.eu.

AIMS Press